INSTITUTE OF PHYSICS PUBLISHING SEMICONDUCTOR SCIENCE AND TECHNOLOGY

Semicond. Sci. Technol. **16** (2001) R41–R49 www.iop.org/Journals/ss PII: S0268-1242(01)16409-6

TOPICAL REVIEW

Structural and vibrational properties of carbon impurities in crystalline silicon

Xiao Yan Zhu[1,2,6], Seung Mi Lee[1,2,7], Jae Yon Kim[1,2], Young Hee Lee[1,2,3,8,9], Dong-Chul Chung[4] and Thomas Frauenheim[5]

[1] Department of Semiconductor Science and Technology, Jeonbuk National University, Jeonju 561–756, Korea
[2] Semiconductor Physics Research Center, Jeonbuk National University, Jeonju 561–756, Korea
[3] Department of Physics, Jeonbuk National University, Jeonju 561–756, Korea
[4] Department of Information and Communication Engineering, Woosuk University, Wanju, 565-701, Korea
[5] Universität-GH Paderborn, Fachbereich Physik, Theoretische Physik, 33095 Paderborn, Germany

E-mail: leeyoung@yurim.skku.ac.kr

Received 16 August 2000, accepted for publication 1 March 2001

Abstract

$Si_{1-x}C_x$ alloys have been studied using self-consistent-charge density-functional-based tight-binding calculations. The origin of experimentally observed carbon-induced vibrational peaks near 475, 607 and 810 cm^{-1} are analysed, based on the theoretical calculations. The stability, vibrational frequencies, lattice relaxations, and energy gap variances of substitutional, interstitial single-carbon and dicarbon complexes in crystalline silicon are calculated. All the impurities induce severe lattice relaxations of adjacent Si atoms. The peak near 475 cm^{-1} originates from the lattice relaxations of Si atoms up to second-nearest neighbours from carbon impurities in all cases. The peak near 605 cm^{-1} originates mainly from the midbond interstitial carbon (which is at odds with general belief) whereas the high-energy peaks near 810 cm^{-1} result from the formation of the carbon complexes.

1. Introduction

The introduction of carbon atoms prior to the deposition of Ge on Si in epitaxial growth to improve the physical properties of SiGe overlayers has recently been the focus of attention. Since the atomic radius of carbon is smaller than that of Si or Ge atoms, codeposition of carbon atoms is expected to release the strain in the SiGe overlayer. The SiGe:C alloy is also expected to extend the bandgap engineering range of SiGe, due to the larger bandgap of diamond, which may provide a possible alternative method for tailoring the electronic properties of the Si system. A high-Ge content is often required to produce a large hole mobility. However, difficulties exist in fabricating high-Ge content SiGe quantum structures, where the Ge atoms segregate easily to the front growth surface during the Si/Ge heteroepitaxial crystal growth. The Ge segregation could be limited by introducing a small amount of carbon atoms during the growth. Outdiffusion of boron atoms which can easily occur at the interface could also be suppressed by forming boron–carbon complexes [1]. Thus, one can expect several advantages with carbon incorporation in SiGe epitaxial growth. Yet, there is a possibility that introducing carbon atoms may be detrimental to the crystal quality and the epitaxial growth conditions. Understanding the effect of carbon atoms in the SiGe system in a systematic way is a prerequisite for further applications.

[6] Present address: Department of Physics, Soochow University, Suzhou 215006, People's Republic of China.
[7] Present address: Fritz Harber Institute, der Max-Planck-Gesellschaft, Faradayweg 4-6, D-14195, Berlin-Dahlem, Germany.
[8] To whom the correspondence should be addressed.
[9] Present address: Department of Physics, Sungkyunkwan University, Suwon, Kyungki 440-746, Korea.

Table 1. Lattice constants and the bulk moduli of crystalline Si, diamond and cubic SiC.

	Lattice constant (Å)	Expt. (Å)[a]	Error (%)	Bulk mudulus (GPa)	Expt. (GPa)[a]	Error (%)
c-Si	5.45	5.43	0.5	96.2	98.8	−1.6%
Diamond	3.56	3.55	0.4	491	443	11.1%
3c-SiC	4.40	4.36	0.9	292	224[b]	30.4%

[a] Taken from [16].
[b] Taken from [17].

Incorporating carbon atoms during Si growth, however, cannot be easily achieved due to the low solid solubility of carbon atoms in Si. Just a few per cent of carbon atoms can be incorporated in Si during the MBE growth. Various carbon-related peaks in Raman spectra have been observed [2,3]. The origin of the side peak at 475 cm^{-1} near the main peak at 520 cm^{-1} is unclear, although it has been suggested that it originates from the disorder at higher carbon concentration [4] and the lattice relaxation of the Si atoms near the substitutional carbon [3]. An additional peak at about 605 cm^{-1} has also been observed in Raman measurements [5–8], and is believed to originate from the substitutional carbon [2]. A new peak near 617 cm^{-1} was observed by Fourier-transform infrared spectroscopy (FTIR) from the chemical vapour deposition-grown samples [9], whose origin was once again assigned to the substitutional carbons. A broad peak near 810 cm^{-1} [5,10–13] and a peak near 725 cm^{-1} [13] are often observed under carbon-rich conditions. All these peaks seem to be related to carbon-induced local geometries. The Si growth with MBC and chemical vapour deposition is a nonequilibrium process, which will lead to the formation of some metastable states in some cases. The substitution carbon impurity is believed to be stable experimentally, whereas the interstitial carbon impurity is a metastable state. The assignment of carbon-related peaks in the Raman and FTIR spectra is somewhat ambiguous. The ambiguity in identifying such observed peaks results mainly from the absence of an appropriate theoretical model.

In order to analyse the origin of the carbon-related vibrational modes, we introduce various structural models of single-carbon and dicarbon complexes in crystalline Si and study the relative stability, structural relaxation, electronic and vibrational properties by using the self-consistent-charge density-functional-based tight-binding method (SCC-DFTB). This paper is organized as follows. In section 2, the general features of the SCC-DFTB method are described. The theoretical structure models and the related structural relaxations and electronic properties are extensively discussed in section 3. In section 4, the vibrational properties are discussed. Charge transfers and impurity states are described in section 5. The origin of the peaks at 475 and 605 cm^{-1}, and near 800 cm^{-1} are discussed in section 6. Finally we conclude our work in section 7.

2. Theoretical approaches

The SCC-DFTB method is a straightforward extension of a typical tight-binding (TB) approach. The SCC-DFTB method uses a basis of numerically obtained s, p and d atomic orbitals. Hamiltonian overlap-matrix elements are evaluated by a two-centre approach, where the interactions extend beyond the first shell of neighbours. Charge transfer is taken into account through the incorporation of a self-consistency scheme for Mulliken charges based on the second-order expansion of the Kohn–Sham energy in terms of charge density fluctuations. The diagonal elements of the Hamiltonian matrix employed are then modified by the charge-dependent contributions in order to describe the change in the atomic potentials due to the charge transfer. The off-diagonal elements have additional charge-dependent terms due to the Coulomb potential of ions. They decay as $1/r$ and thus account for the Madelung energy of the system. Since the self-consistent charge density scheme has been adopted, the charge transfer can be described correctly. This approach is particularly applicable to heterosystems, where the charge transfer plays an important role. Further details of the SCC-DFTB method have been published elsewhere [14].

We use a cubic supercell containing 64 silicon atoms, where the periodic boundary conditions are applied to all x, y and z directions to emulate the bulk silicon. For a single vacancy, one atom is simply removed from the supercell. In the case of the substitutional carbon impurity, one silicon atom is replaced by a carbon atom. One and two carbon atoms are inserted for the interstitial carbons and carbon pair complexes, respectively. The remaining forces with geometry optimization were less than 0.004 Ry in equilibrium. The energy converged to 5.0×10^{-5} au in each self-consistent energy iteration. The convergency was also tested with a larger supercell. With 216 atoms, the total energy difference from 64 atoms was 0.001 eV/atom.

Molecular dynamics (MD) simulations in a microcanonical ensemble are used to calculate the phonon vibrational frequencies [15] with a time step of 3.63×10^{-16} s. The velocities are first rescaled at every step for the first 100 time steps at 300 K. After 500 steps of the microcanonical run, velocity–velocity autocorrelation functions are obtained for the next 18 000 time steps, which correspond to 6 ps, and further Fourier transformed to obtain the vibrational spectra. The convergence was further tested with longer time steps of 10 ps. The difference in the spectral density distribution was negligible.

3. Geometrical models

The validity of our TB parameters is tested by calculating lattice constants and bulk moduli of crystalline Si, diamond and cubic SiC, as shown in table 1. Lattice constants calculated from SCC-DFTB are in excellent agreement with experimental values with errors of less than 1%. Bulk moduli give relatively larger errors, particularly for the cubic SiC, compared with experimental values, although errors are similar to those of calculations using the density functional theory within the local density approximation (LDA). This is expected since our SCC-DFTB parameters were fitted to the LDA calculations. We now

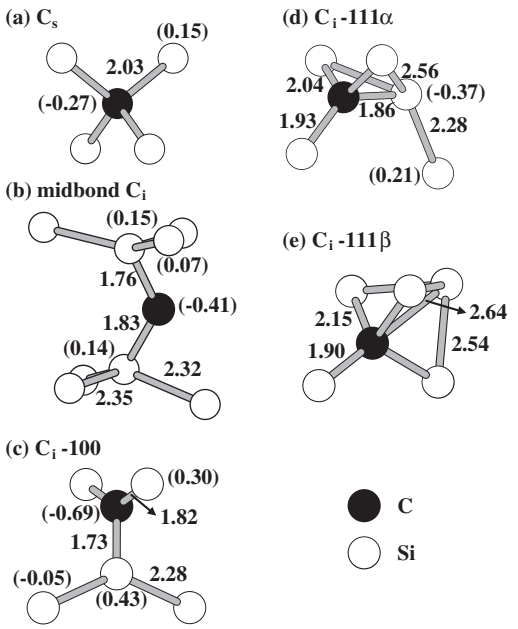

Figure 1. Various geometries of single-carbon impurities; (*a*) substitutional carbon impurity, (*b*) midbond site interstitial carbon impurity, (*c*) C-100 interstitial impurity, (*d*) C-111α interstitial impurity, and (*e*) C-111β interstitial impurity. The black and white balls indicate the C and Si atoms, respectively. All the bond lengths are in units of Å. The charge transfers near the carbon atom are shown in parentheses in electron units, where the amount of charge transfers of magnitude less than 0.05 are not shown in the figure.

consider theoretical models for a single carbon impurity in crystalline Si. Figure 1 shows the local geometries of possible structural models that are fully relaxed in our SCC-DFTB scheme. The formation energy is defined as,

$$E_{\rm form} = E_{\rm total} - N_{\rm C}E_{\rm self}({\rm C}) - N_{\rm Si}E_{\rm self}({\rm Si}) - N_{\rm C}\mu_{\rm C} - N_{\rm Si}\mu_{\rm Si}, \quad (1)$$

where $E_{\rm total}$ is the total energy of the system, and $N_{\rm C}$ and $N_{\rm Si}$ are the number of carbon and silicon atoms, respectively. $E_{\rm self}({\rm C})$ and $E_{\rm self}({\rm Si})$ are atomic self-energies of C and Si, respectively. The chemical potentials of C and Si are represented by $\mu_{\rm C}$ and $\mu_{\rm Si}$, respectively. Bulk Si and diamond are chosen for the chemical potential of Si and C systems for reference. Table 2 summarizes the formation energies of our models. The vacancy formation energy in Si is 3.69 eV, in excellent agreement with experimental results of [10, 19]. Figure 1(*a*) shows the local geometry of the substitutional carbon. The corresponding partial pair-correlation functions are shown in figure 2. The bond length of Si–C is 2.03 Å; longer than that of cubic SiC (1.91 Å). The Si–Si backbonds are extended 2.42 Å from their ideal positions. One should note that this value is very similar to that of an amorphous Si network [20, 21]. The bond angles between the substitutional carbon atom and the adjacent Si neighbours are 110° (as shown in table 3), showing perfect tetrahedral bond angles. The energy is minimized by distorting the bond lengths but not bond angles. The formation energy of the substitutional carbon is 1.7 eV, similar to Tersoff's result [22] but underestimated compared to the experimental value [10, 19].

We next consider various interstitial models, as shown in figures 1(*b*)–(*e*). The midbond interstitial carbon, where

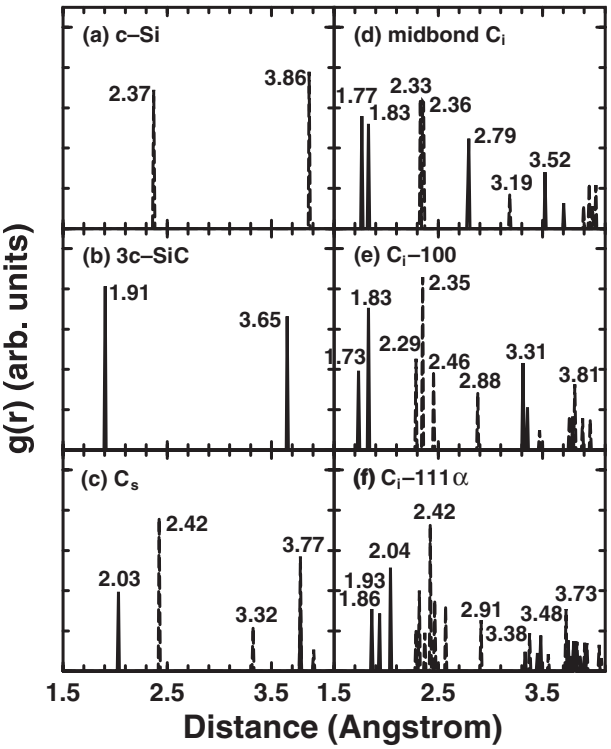

Figure 2. The pair-correlation functions of various structures: (*a*) crystalline Si, and (*b*) 3c-SiC bulk. The partial pair-correlation functions calculated by choosing a carbon atom and its adjacent first nearest-neighbour Si atoms for (*c*) C_s, (*d*) midbond C_i, (*e*) C_i-100, and (*f*) C_i-111α. The solid and long-dashed lines indicate the Si–C and Si–Si distances, respectively. All values are in units of Å.

Table 2. Formation energies (eV) of carbons in crystalline Si.

Type	This work	Tersoff[a]	Expt.[b]
Vacancy	3.69	3.7	3.6 ± 0.2
C_s	1.70	1.6	2.3 ± 0.3
Midbond C_i	5.05	5.3	
C_i-100	4.96	4.6	
C_i-111-α	5.08	5.9	
C_i-111-β	7.52	6.7	
C_s–C_i	5.25		
C_s–C_s	5.19		
C_2-110	5.59		

[a] Taken from [22].
[b] Taken from [18, 19].

carbon takes a midbond between two Si atoms is shown in figure 1(*b*). The midbond carbon pushes backward two adjacent Si atoms which form sp^2 bonds with the adjacent Si atoms. The Si–C bond lengths are asymmetric with values of 1.76 and 1.83 Å, shorter than 1.91 Å of cubic SiC, and the Si backbonds are not distorted much from their ideal positions, in good contrast with the interstitial carbon in figure 1(*a*). The bond angle around the midbond carbon atom is as large as 124°, nearly forming sp^2 rehybridization. We note that this asymmetric midbond carbon is more stable than the symmetric one by 0.3 eV.

One can also consider a midbond carbon along the [100] direction. The fully relaxed C_i-100 is shown in figure 1(*c*), where the carbon atom shares with three adjacent Si atoms in this case, with bond lengths of 1.73 and 1.82 Å. This

Table 3. Bond angles around the carbon impurities. C_3 and C_4 indicate the three-folded and four-folded carbon atoms respectively. Si_2, Si_3 and Si_4 indicate the two-folded, three-folded, and four-folded silicon atoms, respectively.

C_s	$\theta_{Si_4-C_4-Si_4}$ 110°				
Midbond C_i	$\theta_{Si_4-C_2-Si_4}$ 124°				
C_i-100	$\theta_{Si_4-C_3-Si_4}$ 144°	$\theta_{Si_4-C_3-Si_3}$ 108°			
C_i-111-α	$\theta_{Si_5-C_4-Si_5}$ 121°	$\theta_{Si_5-C_4-Si_4}$ 116° 82°	$\theta_{Si_4-C_4-Si_4}$ 132°		
C_s–C_i	$\theta_{Si_4-C_4-Si_4}$ 117° 113°	$\theta_{Si_4-C_4-Si_3}$ 110° 102°	$\theta_{Si_4-C_3-Si_4}$ 130°	$\theta_{Si_4-C_3-Si_3}$ 104°	$\theta_{C_4-Si_3-C_3}$ 111°
C_s–C_s	$\theta_{Si_4-C_4-Si_4}$ 114° 115° 115° 117°	$\theta_{Si_4-C_4-Si_2}$ 81° 114° 131° 86°	$\theta_{C_4-Si_2-C_4}$ 122°		
C_2-110	$\theta_{Si_4-C_3-Si_4}$ 150°	$\theta_{Si_4-C_3-C_2}$ 100° 111°	$\theta_{C_3-C_2-Si_5}$ 113°		

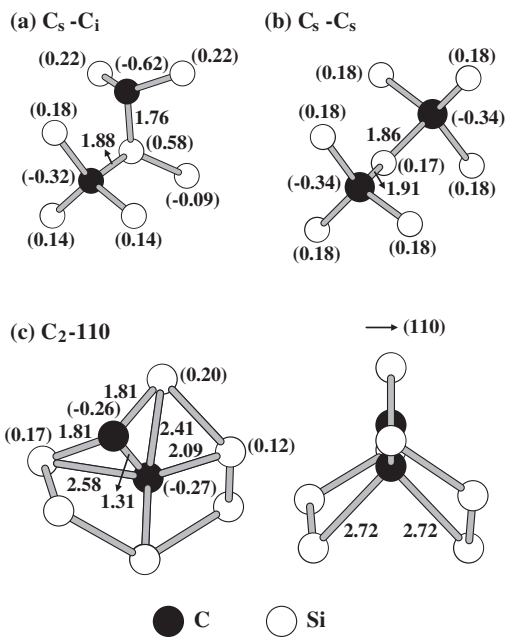

Figure 3. Various geometries of dicarbon complexes; (*a*) C_i–C_s complex, (*b*) C_s–C_s complex, and (*c*) C_2-110 complex. The black and white balls indicate the C and Si atoms, respectively. All the bond lengths are in units of Å. The excess charge transfers are shown in parentheses in electron units.

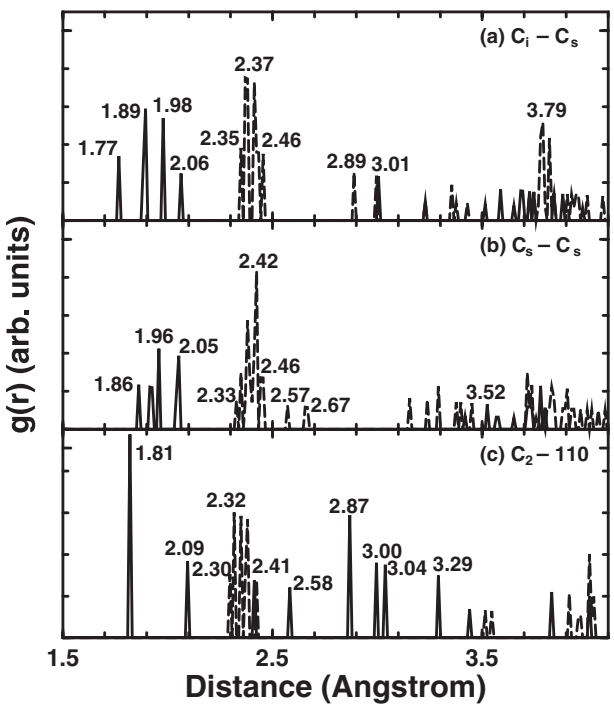

Figure 4. The partial pair-correlation functions calculated by choosing carbon atoms and the adjacent first nearest-neighbour Si atoms for (*a*) C_i–C_s complex, (*b*) C_s–C_s complex, and (*C*) C_2-110 complex. The solid and the long dashed lines indicate the Si–C and Si–Si distances, respectively. All values are in units of Å.

carbon induces severe contractions in its vicinity, giving rise to the second-nearest-neighbour distances of 2.88 Å, much shorter than that of 3.86 Å in ideal crystalline Si. Some Si–Si backbonds are shortened to 2.29 Å, whereas some are extended to 2.46 Å, as shown in figure 2(*e*). This geometry is similar to that obtained from *ab initio* results [23, 24](see table 4) with an error of near C_i-100 of 2.7% at most. The bond angles around the carbon atom are 108 and 144°, respectively. This also induces severe bond angle distortions of the underlying Si atom. The formation energy of C_i-100 is slightly smaller than that of midbond C_i by 0.09 eV.

One may also introduce a tetrahedral carbon along the [111] direction, C_i-111α. However, the tetrahedral position is unstable after full relaxation. Instead, the carbon atoms form bonds with their three Si neighbours with bond lengths of 1.86, 1.93 and 2.04 Å, as shown in figure 1(*d*). This leads to stretching of the Si–Si backbonds, as appears in the pair-correlation function presented in figure 2(*f*). The bond angles around the carbon atom vary from 82° to 132°. The formation energy is similar to the previous ones. We further tried the similar configuration, C_i-111β, as shown in figure 1(*e*) but the formation energy was too high, as listed in table 2. Therefore, this configuration will not be discussed in the following discussion.

For the dicarbon complexes in crystalline Si, we consider a combination of two single-carbon impurities. Figure 3(*a*) shows the C_s–C_i complex, where one carbon atom takes the substitutional position, and the other carbon atom takes an interstitial position near the substitutional carbon, mediated by one Si atom. The Si–C bonds are spread from 1.77 to

Table 4. Geometrical data of midbond C_i, C_i–C_s and C_s–C_s in comparison with *ab initio* results. The indices are the same as in table 3. All the bond lengths are in units of Å.

	C_3-Si_3	C_3-Si_4	Si_3–Si_4	$\theta_{Si_4-C_3-Si_4}$	$\theta_{Si_4-C_3-Si_3}$
C_i-100[a]	1.77	1.80	2.22	157°	122°
C_i-100[b]	1.728	1.820	2.300	137°	125°
C_i-100	1.73	1.82	2.28	144°	108°
	C_4–Si_4	C_4–Si_3	C_3–Si_3	C_3–Si_4	Si_3–Si_4
C_i–C_s[b]	2.007 2.075	1.846	1.708	1.855	2.352
C_i–C_s[c]	1.984 2.032	1.853	1.726	1.825	2.342
C_i–C_s	1.98 2.06	1.88	1.76	1.89	2.41
	C_4–Si_4	C_4–Si_2	$\theta_{C_4-Si_2-C_4}$		
C_s–C_s[b]	1.960 2.330 2.043 1.970	1.831 1.819	126°		
C_s–C_s[c]	1.950 2.083 2.026 1.931	1.833 1.805	127°		
C_s–C_s	1.96 2.04 2.06 1.93	1.91 1.86	122°		

[a] Taken from [23].
[b] Taken from [24].
[c] Taken from [25].

2.06 Å. This configuration provides less distortions in the Si–Si backbonds, as can be seen from figure 4(*a*), where the Si–Si bond lengths near the carbon atoms are about 2.37 Å, close to the ideal Si–Si bond length. This configuration is compared with the previous *ab initio* calculations [24, 25], as shown in table 4. The error is less than 3.6%. Carbon-related bond angles vary from 102° to 130 °. On average the midbond Si atom between two carbon atoms has a severe bond angle of 120°. The formation energy of the C_i–C_s complex is 5.25 eV, comparable to that of single carbon impurities (midbond C_i and C_i-111α). This value is smaller than the sum of C_s and any C_i formation energies, suggesting that at high temperature they are likely to form complexes.

One can also consider the C_s–C_s complex, as shown in figure 3(*b*), where two C_s are intermediated by a single Si atom. The Si–C bond lengths are spread in the range 1.86–2.05 Å, similar to those in the C_s–C_i complex. However, the Si–Si backbonds are more severely distorted than those in the C_s–C_i complex, as can be seen from figure 4(*b*). Various bond angles around the carbon atoms are shown in table 3. We can see clear carbon atom rehydridization to sp^2+p from sp^3. The formation energy is 5.19 eV, slightly lower by 0.06 eV than that of the C_s–C_i complex. One can simply estimate the relative energetics by bond counting. In the case of the C_s–C_i complex, there are seven Si–C bonds and one Si–Si bond in the local region of the complex, while the C_s–C_s complex has eight Si–C bonds and no Si–Si bond. It is expected that the C_s–C_s complex should give a lower formation energy by a value of E_b(Si–C)$-E_b$(Si–Si), which is about 1.2 eV. However, the energy gain obtained by the bond-counting is almost entirely dissipated by the large strain energy accommodated in the Si–Si backbonds. The resultant energy difference between the two complexes is only 0.06 eV, similar to the *ab initio* results [24, 25] (see table 4).

Another carbon-pair complex, C_2-110, is shown in figure 3(*c*). One carbon breaks into two Si bonds and another carbon is located almost at the hexagonal centre. The two carbon atoms with the adjacent Si atoms are situated in the (110) plane. The strong C–C bond is formed with a bond length of 1.31 Å. This does not induce severe lattice distortions in Si–Si backbonds, as shown in figure 4(*c*). The carbon-related bond angles are listed in table 3. The formation energy of this configuration is 5.59 eV, slightly higher than those of the previous ones. We also tried the C_2 dimer complex at the interstitial position but the formation energy was 9.8 eV, too high to be considered even for a high carbon concentration in Si.

4. Vibrational frequencies

In order to correlate the structural properties of carbon impurities with vibrational frequencies in conjunction with experimentally observed Raman and FTIR measurements, here we calculate the vibrational frequencies using the velocity–velocity autocorrelation function in MD simulations. The vibrational frequency is calculated by taking the Fourier transform of the velocity–velocity autocorrelation function,

$$f(\omega) = \int_0^\infty \mathrm{e}^{\mathrm{i}\omega t} f(t)\,\mathrm{d}t \tag{2}$$

$$f(t) = \sum_i^N \sum_{t=0}^\infty \vec{v}_\mathrm{i}(0) \cdot \vec{v}_\mathrm{i}(t). \tag{3}$$

Here $\vec{v}_\mathrm{i}\ (t)$ is the velocity of the ith atom at time t. The partial phonon spectrum can be obtained by choosing some specific atoms in the system. We first calculate the phonon spectrum for pure Si, as shown in the top panel of figure 5(*a*) with a long-dashed line. The strong peak appears at 495 cm^{-1}, which is underestimated by 5%, compared to the experimental value of 520 cm^{-1}. The solid line in the top panel shows a partial phonon spectrum of the C_s, where the carbon atom and the nearest-neighbour Si atoms are chosen only. The strong peak at 485 cm^{-1} is localized in the Si–Si backbonds, as can be seen from the bottom panel. The vibrational strength of the carbon peak is relatively weak at 546 cm^{-1}. This may be attributed to weaker Si–C bonds (2.03 Å).

The partial phonon spectrum looks more complicated in the case of the midbond interstitial carbon, which is shown in figure 5(*b*). Strong carbon-confined peaks appear at 633 and 991 cm^{-1}. Some side peaks appear in the lower-energy side below 495 cm^{-1} from the Si–Si backbonds. The small intensity peak at 633 cm^{-1} in the third panel of figure 5(*b*) is induced by the adjacent carbon atom. In the case of the C_i-100, carbon-confined peaks of three normal modes appear at 843,

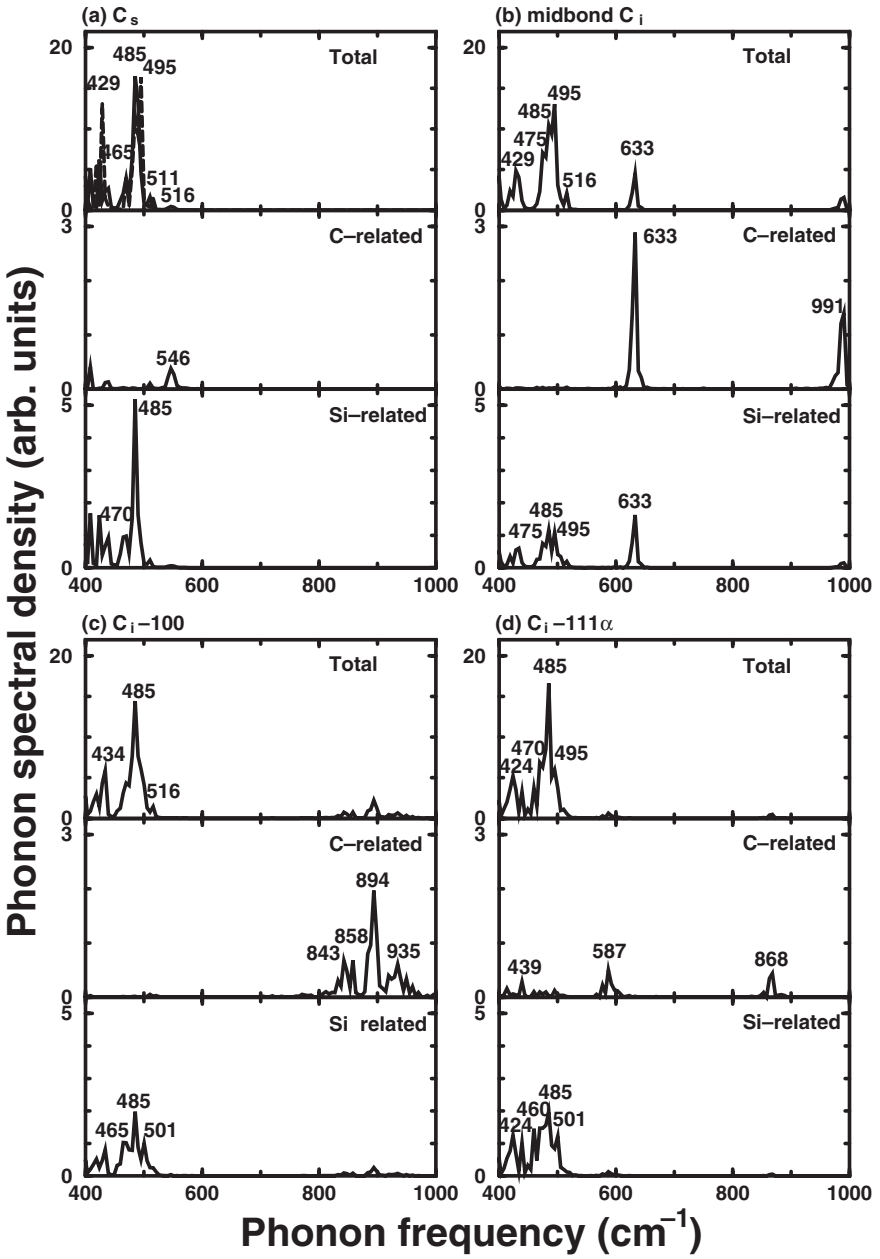

Figure 5. The local phonon spectral densities for various single-carbon impurities of (*a*) C_s, (*b*) midbond C_i, (*c*) C_i-100, and (*d*) C_i-111α. The top, middle and bottom panels show the phonon spectra of the whole supercell, carbon-related peaks, and the first nearest-neighbour Si-related peaks, respectively. All the values are in units of cm^{-1}. The long-dashed line indicates the phonon spectral density of bulk Si as a reference.

894 and 935 cm^{-1}. These are comparable to the previously calculated values of 867 and 935 cm^{-1} by density functional cluster approaches [24]. It is not clear at this point whether this small discrepancy comes from the cluster calculations or from our TB approach. The peaks near 485 cm^{-1} are again attributed to Si–Si backbonds. The C_i-111α also shows peaks near 485 cm^{-1}, but relatively small carbon-related peaks near 587 and 868 cm^{-1}. Note that all these configurations consistently give peaks near 485 cm^{-1}, whereas the peak positions of carbon-confined peaks vary with different configurations. The carbon-related peak positions are strongly correlated to the C–Si bond strengths, as indicated by the pair-correlation functions presented in figure 3.

Figure 6 shows the partial phonon spectra for dicarbon complexes. All dicarbon complexes give relatively weak peak strengths near 480 cm^{-1}. Several carbon-related peaks at 572, 802, 848 and 919 cm^{-1} appear in the case of the C_i–C_s complex. In fact, the peak at 572 cm^{-1} is in good agreement with the experimentally observed value of 579.5 cm^{-1} [26]. The calculated high-frequency modes are overestimated compared to the previously reported values which range from 543 to 838 cm^{-1} [24]. The six carbon-related normal modes appear in a more complicated way in case of the C_s–C_s complex, as can be seen in the middle panel of figure 6(*b*). The low-frequency mode at 552 cm^{-1} is in excellent agreement with the previously calculated value [24], although high-frequency modes spread

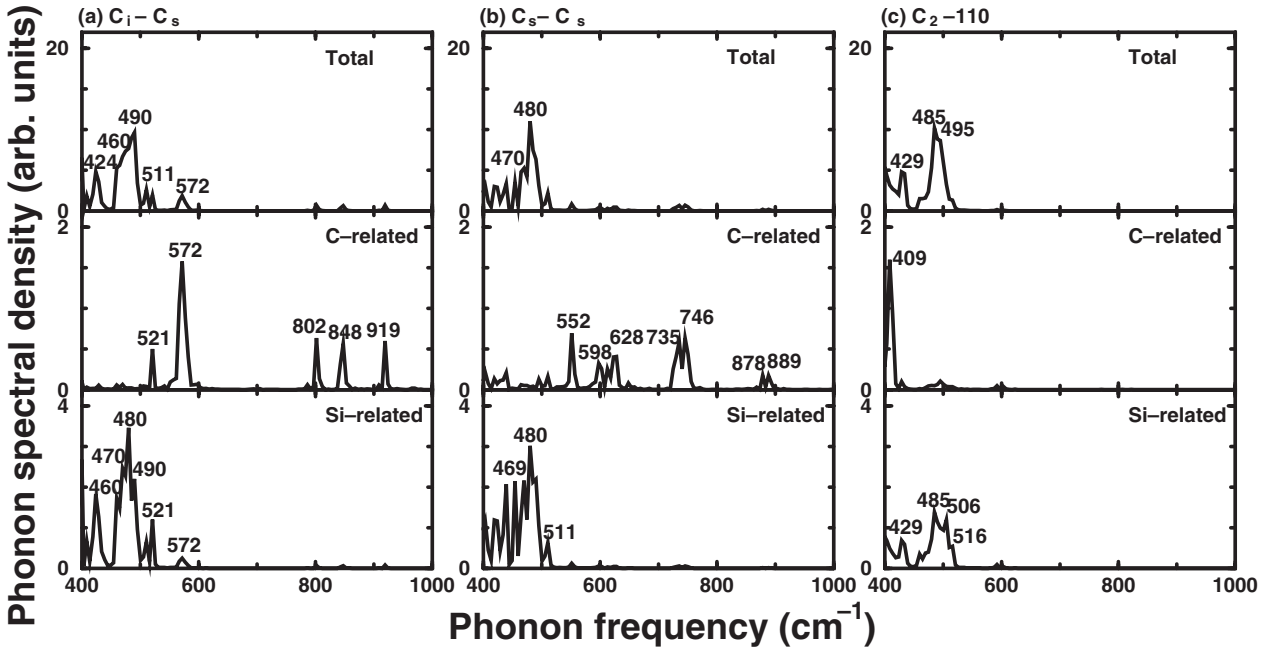

Figure 6. The local phonon spectral densities of various dicarbon impurities, similar to figure 8 for (*a*) the C_i–C_s complex, (*b*) the C_s–C_s complex and (*c*) the C_2-110 complex.

over 735–746 cm^{-1} and 878–889 cm^{-1}, compared to the previously reported value of 649 cm^{-1}. We note that our approach produces all the eigenmodes from molecular dynamics calculations, whereas the previous calculations are frozen-phonon calculations performed using the dynamical matrix. In the case of the carbon-pair complex (C_2-110), peaks at 485 cm^{-1} appear but no carbon-related peaks are shown in figure 6(*c*).

5. Charge transfers and impurity states

Since the carbon atom has a higher electronegativity than the silicon atom, it is expected to exert a strong charge transfer effect directed from the silicon atom to the carbon atom. In general, the traditional TB approach does not describe the charge transfer accurately, particularly for heterosystems. Our SCC-DFTB method calculates the charge self-consistently and therefore we expect the charge transfer to be accurately described in our scheme. Numbers in parentheses in figures 1 and 3 indicate the actual Mulliken excess charges in electron units. The carbon atom in the substitutional site takes extra electrons from its adjacent Si atoms, forming partially ionic bonds and yet the tetrahedral symmetry is preserved. Thus, we expect that the C_s peaks are Raman-active but not IR-active.

Charge transfer occurs to a greater extent in the midbond carbon, as shown in figure 1(*b*), where charges are depleted from the first- and second-nearest neighbouring Si atoms. Note that the midbond carbon atom is asymmetric, forming permanent dipole moments. We therefore expect that the midbond-carbon related peaks are both Raman- and IR-active. The peak near 633 cm^{-1} should be observable with Raman and IR measurements. The carbon atom in C_i-100 configuration holds even larger excess charges than the midbond interstitial carbon. It suggest that carbon-related peaks near 894 cm^{-1} and Si–Si backbond-related peaks near 485 cm^{-1} should be more easily detected in IR and Raman measurements than other configurations. The carbon atom in the C_i-111α does not hold any extra charge but instead the adjacent Si atoms unexpectedly possess the extra charges, where these Si atoms are now five-coordinated with the extra charges. Therefore, the peak near 485 cm^{-1} originating from the Si–Si backbonds should be more IR-active.

The charge transfers become more severe in the dicarbon complexes. As shown in figure 3(*a*), the interstitial carbon atom holds −0.62 e and the substitutional carbon holds −0.32 e, where charge on the intermediated Si atom (0.58 e) is mostly depleted. If the C_i–C_s complex is formed in the network, this should be strongly active with IR measurement and contribute to peaks near 485 cm^{-1} and several carbon-related peaks just over 800 cm^{-1}. We expect that high-frequency regions over 800 cm^{-1} should be observable with both Raman and IR measurements. Less severe charge transfer also occurs in the C_s–C_s complex. Although the C_2-110 complex is as stable as other complexes, the charge transfer is not so significant and is probably unlikely to be observable with IR measurements.

Introducing carbon impurities in the SiGe growth changes not only the growth kinetics but also the electronic and optical properties of the system. Figure 7 shows the carbon impurity levels, where the top valence band is taken as a reference. The bandgap of bulk Si is 1.29 eV, a little larger than the experimental value of 1.12 eV. This overestimation results from the small sizes of the basis sets, which basically poorly describe the conduction band. We next calculate carbon-impurity levels by calculating the local density of states. The substitutional carbon gives rise to a shallow unoccupied level at 1.09 eV. The asymmetric midbond C_i contributes to the shallow unoccupied and occupied levels at 1.05 and 0.04 eV, respectively. The C_i-100 configuration has a deep occupied level at 0.98 eV and a shallow one at 0.06 eV. The dicarbon complexes contribute

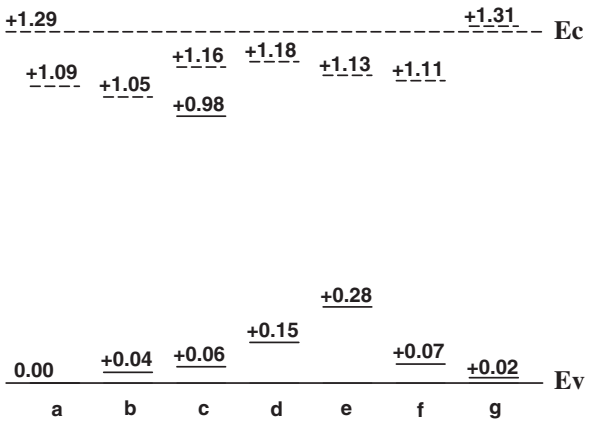

Figure 7. The impurity levels at the band gap for various carbon impurities of (*a*) C_s, (*b*) midbond C_i, (*c*) C_i-100, (*d*) C_i-111α, (*e*) C_i–C_s complex, (*f*) C_s–C_s complex, and (*g*) C_2-110 complex. The solid- and long-dashed lines indicate occupied and unoccupied states, respectively. All values are in units of eV.

mainly to the deep occupied states and shallow unoccupied states. The C_i–C_s complex contributes to the much deeper occupied states at 0.28 eV which is deeper than *ab initio* result [27], whereas the C_s–C_s complex contributes to the relatively shallow gap states in comparison with *ab initio* calculation [27]. It is known that the carbon impurity in Si is a deep donor [28]. This is true for the single-carbon impurity or with small carbon concentrations. However, with increasing carbon concentrations, one can expect carbon complexes to be formed and therefore deep acceptors can be also formed, as shown in figure 7.

6. Discussion

We now discuss the origin of peaks at 475 and 605 cm^{-1}, and the peak near 810 cm^{-1}, which was observed in the Raman and FTIR spectra. All single and dicarbon impurities have local Si-related vibrational modes near 485 cm^{-1}, corresponding to the experimental peak at 475 cm^{-1}. This peak originates from the Si lattice distortions near carbon atom(s), more specifically lattice extensions of the adjacent Si atoms near to 2.42 Å, close to the bond length of the amorphous Si network [20, 21]. Si backbonds in the C_s and C_s–C_s complex are mostly extended to 2.42 Å, as shown in figure 4(*c*), while the Si backbonds in other impurities are shortened or extended. The phonon spectral intensity from Si backbonds in C_s is stronger than others.

The origin of the peak near 605 cm^{-1} seems to be more complicated. Although the extension of Si backbonds in the C_s mostly contributes to the 475 cm^{-1}, the local carbon peak at 546 cm^{-1} shows relatively weak intensity, as shown in figure 5(*a*). It is thus difficult to attribute this as being the origin of the peak at 605 cm^{-1}. However, the midbond C_i has a strong peak at 633 cm^{-1}, which can be attributed as the origin of the peak at 605 cm^{-1}, although the lattice distortion is less severe than that of C_s. The formation energy of the midbond C_i is 5.05 eV, which is much greater than that of C_s, but this difference will vary with a reference of chemical potentials for Si and C systems. Therefore it may be concluded that the C_s and the midbond C_i may coexist in the sample. Furthermore, the carbon-related peak at 605 cm^{-1} has previously been observed in IR measurements [13, 29]. From our arguments, we conclude that it is the midbond interstitial carbon that was observed in the IR measurement. There is also a possibility that C_i-111α contributes to the peak near 605 cm^{-1} but this possibility may be excluded, since the intensity at 587 cm^{-1} is relatively small, as shown in figure 5(*d*). The C_s–C_s complex may also contribute to the peak near 605 cm^{-1}, as shown in figure 6(*b*), where the frequency spreads in over a wide range. The C_s cannot generate the peak at 605 cm^{-1} as discussed above. Instead some metastable carbons such as various interstitial carbons may be formed at such low growth temperature, which give rise to the peak near 605 cm^{-1}. It is believed that carbon atoms are directly attached to the growing surface sites with low surface diffusion due to the low surface diffusivity of carbon below 500 °C [30]. In a kinetically limited growth process in such a low-temperature region, the arriving carbon adatoms become rapidly buried in the near-surface region and then immobilized. This leads to an increased carbon surface solubility, which has been known to play an important role in achieving a sufficiently high carbon content in $Si_{1-x}C_x$ alloys even though carbon has a very low bulk solubility in Si and Ge [31]. With increasing annealing temperatures, the Si network becomes fully relaxed, accelerating the formation of the crystalline phase indicated by the zone-centre peak at 520 cm^{-1} and thus the peak near 475 cm^{-1} diminishes. The small bump at the lower-energy side near 520 cm^{-1} still remains even at a high annealing temperature of 600 °C [13, 29]. The Si network must be completely relaxed in order to have a crystalline phase but particularly those silicons around substitutional carbons still have extended Si–Si bonds, contributing to the amorphous-like peak near 475 cm^{-1}. At high-temperature annealing above 750 °C [29], the high-energy peak near 810 cm^{-1} appears. At this annealing temperature, carbon atoms can be kinetically activated, promoting the carbon diffusion in the Si network. This leads to the formation of substitutional carbons as well as some interstitial carbons, and furthermore the C_s–C_s and C_i–C_s complexes. In fact, the C_s–C_s complex gives similar local geometries to the 3*C*–SiC.

7. Conclusion

Vibrational properties associated with structural properties are interpreted in conjunction with SCC-DFTB total energy calculation results combined with a molecular-dynamics simulation technique. From our analysis we conclude the following: (i) the peak near 475 cm^{-1} originates from the lattice stretchings of Si backbonds around carbon impurities and is contributed to by all the carbon impurities discussed above, (ii) the peak near 605 cm^{-1} originates mainly from the midbond interstitial carbons, (iii) at high growth temperature or high annealing temperature, even the C_s–C_s complex can contribute to the peak broadening near or above 605 cm^{-1}, (iv) at high annealing temperature, the C_i–C_s and C_s–C_s complexes form and precipitation of SiC can take place: both contribute to the high-frequency peak near 810 cm^{-1}, and (v) most single-carbon impurities contribute to the shallow gap states, whereas the C_i–C_s and C_s–C_s complexes contribute to the deep-gap states.

References

[1] Osten H J, Barth R, Fischer G, Heinemann B, Knoll D, Lippert G, Rücher H, Schley P and Röpke W 1998 *Thin Solid Films* **321** 11

[2] Eberl K, Iyer S S, Zollner S, Tsang J C and LeGoues F K 1992 *Appl. Phys. Lett.* **60** 3033

[3] Tsang J C, Eberl K, Zollner S and Iyer S S 1992 *Appl. Phys. Lett.* **61** 961

[4] Forman R, Bell M I, Myers D R and Chandler-Horowitz D 1985 *Japan. J. Appl. Phys.* **10** L848

[5] Strane J W, Stein H J, Lee S R, Picraux S T, Watanabe J K and Mayer J W 1994 *J. Appl. Phys.* **76** 3656

[6] Rücker H, Methfessel M, Dietrich B, Pressel K and Osten H J 1996 *Phys. Rev.* B **53** 1302

[7] Guedj C, Portier X, Hairie A, Bouchier D, Calvarin G and Piriou B 1997 *Thin Solid Films* **294** 129

[8] Melendez-Lira M, Melendez J, Kramer K M, Thompson M O, Cave N, Liu R, Christiansen J W, Theodore N D and Candelaria J J 1997 *J. Appl. Phys.* **82** 4246

[9] Chandrasekhar D, McMurran J, Smith D J, Kouvetakis J, Lorentzen J D and Menéndez J 1998 *Appl. Phys. Lett.* **72** 2117

[10] Bean A R and Newman R C 1971 *J. Phys. Chem. Solids* **33** 255

[11] Osten H J, Kim M, Pressel K and Zaumseil P 1996 *J. Appl. Phys.* **80** 6711

[12] Warren P, Mi J, Overney F and Dutoit M 1995 *J. Cryst. Growth* **157** 414

[13] Dashiell M W, Kulik L V, Hits D and Kolodzey J 1998 *Appl. Phys. Lett.* **72** 833

[14] Elstner M, Porezag D, Jungnickel G, Elsner J, Haugk M, Frauenheim Th, Suhai S and Seifert G 1998 *Phys. Rev.* B **58** 7260

[15] Wang C Z, Chan C T and Ho K M 1989 *Phys. Rev.* B **39** 8586

[16] Data in Science and Technology 1991 *Semiconductor Group IV Elements and III–V Compounds* (Berlin: Springer)

[17] Yean D H and Riter J R 1971 *J. Phys. Chem. Solids* **32** 653

[18] Bean A R *et al* 1997 *J. Phys. Chem. Solids* **32** 1211

[19] Dannefaer S *et al* 1986 *Phys. Rev. Lett.* **56** 2195

[20] Kim E and Lee Y H 1994 *Phys. Rev.* B **49** 1743

[21] Kim E and Lee Y H 1995 *Phys. Rev.* B **51** 5429

[22] Tersoff J 1990 *Phys. Rev. Lett.* **64** 1757

[23] Capaz R B, Dal A P Jr and Joannopoulos J D 1994 *Phys. Rev.* B **50** 7439

[24] Leary P, Jones R, Oberg S and Torres V J B 1997 *Phys. Rev.* B **55** 2188

[25] Capaz R B, Dal A P Jr and Joannopoulos J D 1998 *Phys. Rev.* B **58** 9845

[26] Davies G and Newman R C 1994 *Handbook on Semiconductors* vol 3, ed S Mahajan (New York: Elsevier) p 1557

[27] Song L W, Zhan X D, Benson B W and Watkins G D 1990 *Phys. Rev.* B **42** 5765

[28] Sze S M 1981 *Physics of Semiconductor Devices* (New York: Wiley) p 21 and references therein

[29] Guedj C, Dashiell M W, Kulik L, Kolodzey J and Hairie A 1998 *J. Appl. Phys.* **84** 4631

[30] Joelsson K B, Ni W-X, Ponzina G, Radamson H H and Hansson G V 1997 *Appl. Phys. Lett.* **71** 653

[31] Tersoff J 1995 *Phys. Rev. Lett.* **74** 5080